Statistical Test for Diffusion-Based Anomaly Localization via Selective Inference

Anonymous authors
Paper under double-blind review

Abstract

Anomaly localization in images—identifying regions that deviate from normal patterns—is vital in applications such as medical diagnosis and industrial inspection. A recent trend is the use of image generation models in anomaly localization, where these models generate normal-looking counterparts of anomalous images, thereby allowing flexible and adaptive anomaly localization. However, these methods inherit the uncertainty and bias implicitly embedded in the employed generative model, raising concerns about the reliability. To address this, we propose a statistical framework based on selective inference to quantify the significance of detected anomalous regions. Our method provides p-values to assess the false positive detection rates, providing a principled measure of reliability. As a proof of concept, we consider anomaly localization using a diffusion model and its applications to medical diagnoses and industrial inspections. The results indicate that the proposed method effectively controls the risk of false positive detection, supporting its use in high-stakes decision-making tasks.

1 Introduction

Anomaly localization using image generation models, particularly diffusion models, has shown great promise across diverse domains such as medical diagnosis and industrial inspection (Li et al., 2023; Iqbal et al., 2023; Lu et al., 2023; Zhang et al., 2023; Fontanella et al., 2024; Tebbe & Tayyub, 2024; Sheng et al., 2024). These models reconstruct *a normal-looking version* of an input image, and differences between the input and the reconstruction highlight potential anomalies. Compared to traditional anomaly localization methods, generative approaches are highly suitable for settings where annotations for anomalous regions are unavailable. Moreover, generative approaches can flexibly handle heterogeneity by adapting to individual images—e.g., patient-specific characteristics in medical diagnosis and product-specific traits in industrial inspection. Among various image generation models, diffusion models, in particular, offer high fidelity and stability, often outperforming other methods in image quality and anomaly localization.

While generative approaches offer powerful and flexible capabilities for anomaly localization, a major concern is that the inherent uncertainty and bias in generative models can affect localization performance (Fithian et al., 2014; Taylor & Tibshirani, 2015; Lee et al., 2016; Duy & Takeuchi, 2022; Miwa et al., 2023; Shiraishi et al., 2024). These models are trained on specific datasets composed of normal images, and the quality of the generated normal-looking images depends heavily on the dataset distribution and how accurately the model has learned it. As a result, uncertainties or biases in the dataset or training process can cause incorrect reconstructions, leading to inaccurate localizations and misidentification of anomalies. Such risks are especially critical in high-stakes domains such as medical diagnosis and industrial inspection, where even minor errors can have serious consequences. Therefore, it is essential to incorporate a rigorous uncertainty quantification framework and statistical safeguards to ensure reliable deployment in critical applications.

To address this issue, we propose a statistical testing framework based on Selective Inference (SI) to assess the statistical significance of detected anomalies. SI has emerged as a promising approach for conducting statistical inference on hypotheses that are selected based on observed data. In this framework, inference is performed using the conditional distribution given the selection event, thereby accounting for the uncertainty

and bias associated with the hypothesis selection. Following this SI framework, our key idea is to apply statistical testing to detected anomalies, conditioned on the fact that the anomalous regions were identified using a specific generative model. This allows us to quantify the statistical significance of detected anomalies as a valid p-value, providing a rigorous estimate of the false positive rate and offering a principled metric for reliability.

In this paper, as a proof of concept for the proposed statistical testing framework, we focus on a standard *denoising diffusion probabilistic model (DDPM)* (Ho et al., 2020; Song et al., 2022) among various diffusion-based anomaly detection (AD) methods, and demonstrate its applications to medical diagnostics and industrial inspections. However, the proposed framework is readily generalizable to a broader range of diffusion model architectures and is applicable to semi-supervised AD problems in other domains.

Related works Diffusion models have been effectively utilized in anomaly localization problems (Pinaya et al., 2022; Fontanella et al., 2024; Wyatt et al., 2022; Mousakhan et al., 2023). In this context, the *DDPM* is commonly used (Ho et al., 2020; Song et al., 2022). During the training phase, a DDPM model learns the distribution of normal medical images by iteratively adding and then removing noise. In the test phase, the model attempts to reconstruct a new test image. If the image contains anomalous regions, such as tumors, the model may struggle to accurately reconstruct these regions, as it has been trained primarily on normal regions. The discrepancies between the original and the reconstructed image are then analyzed to identify and highlight anomalous regions. Other types of generative models have also been used for the anomaly localization task (Baur et al., 2021; Chen & Konukoglu, 2018; Chow et al., 2020; Jana et al., 2022).

SI was first introduced within the context of reliability evaluation for linear model features when they were selected using a feature selection algorithm (Lee & Taylor, 2014; Lee et al., 2016; Tibshirani et al., 2016), and then extended to more complex feature selection methods (Yang et al., 2016; Suzumura et al., 2017; Hyun et al., 2018; Rügamer & Greven, 2020; Das et al., 2021). Then, SI proves valuable not only for feature selection problems but also for statistical inference across various data-driven hypotheses, including unsupervised learning tasks (Chen & Bien, 2020; Tsukurimichi et al., 2021; Tanizaki et al., 2020; Duy et al., 2022; Le Duy et al., 2024; Lee et al., 2015; Gao et al., 2022; Duy et al., 2020; Jewell et al., 2022). The fundamental idea of SI is to perform inference conditional on the hypothesis selection event, which mitigates the selection bias issue even when the hypothesis is selected and tested using the same data. To conduct SI, it is necessary to derive the sampling distribution of the test statistic conditional on the hypothesis selection event. To the best of our knowledge, SI was applied to statistical inferences on several deep learning models (Duy et al., 2022; Miwa et al., 2023; Shiraishi et al., 2024; Miwa et al., 2024), but none of these works addresses image generation by diffusion models.

Contributions The main contributions of our study are summarized as follows[1].

- We propose a novel statistical testing framework to assess the significance of anomaly localization results obtained from diffusion model-based methods, offering a principled basis for evaluating the reliability of detected anomalies.
- We implement the SI framework for diffusion models by deriving the sampling distribution conditional on the selection event induced by the diffusion model, which requires developing non-trivial computational techniques tailored to the generative sampling process.
- We provide theoretical justification for the proposed method and validate its effectiveness through extensive numerical experiments in medical diagnosis and industrial inspection scenarios. The results highlight the robustness and practical utility of our method.

The implementation code for reproducing all experimental results is provided as supplementary material.

[1]We note that our contribution is *not* the development of a new diffusion-based anomaly localization algorithm, but rather the introduction of a rigorous statistical testing framework designed to quantify the statistical reliability of anomalous regions identified by diffusion-based AD methods.

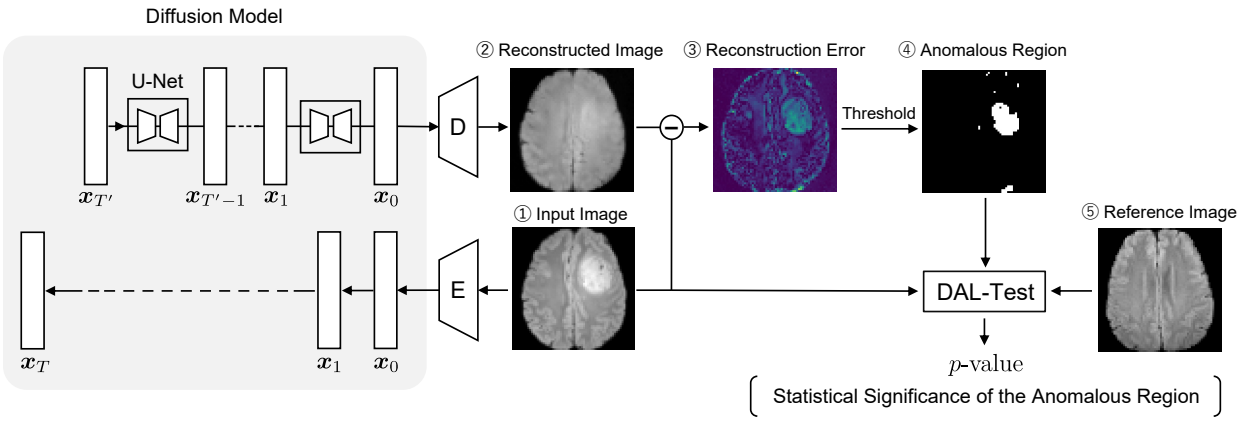

Figure 1: Schematic illustration of anomaly localization using a diffusion model and the proposed DAL-Test. When a test image—potentially containing an anomalous region—is fed into a trained diffusion model, its normal-looking version is generated through the forward and reverse processes. By comparing the input image with the generated normal-looking version, the anomalous region can be identified. We propose the *Diffusion-based Anomaly Localization (DAL) Test*, which leverages the selective inference framework to compute valid p-values that quantify the statistical significance of anomalous regions detected by a diffusion model, based on a test statistic defined over the input and reference images.

2 Anomaly localization by diffusion models

This section describes the anomaly localization task based on a diffusion model, which is explored as a proof of concept in this study. The process of anomaly localization using generative models can generally be divided into two phases. First, during the training phase, a denoising diffusion probabilistic model (DDPM) is trained using a dataset composed exclusively of normal images. The model learns the distribution of normal images through two key processes: the diffusion process, in which noise is gradually added to an image, and the reverse diffusion process, in which the original image is reconstructed from noise. Through this procedure, the model enhances its capacity to reconstruct normal image structures by acquiring denoising capabilities at each step. Next, during the testing phase, the reverse diffusion process is conditionally applied to an unseen input test image. In this step, the model reconstructs an image that closely resembles the input but conforms to its learned notion of "normality", causing anomalous regions to be poorly reproduced. An anomaly score is then computed based on the difference between the reconstructed image and the input test image, and the spatial distribution of this score is analyzed to localize anomalies. By applying thresholding to the score map, anomalous regions can be identified.

In this study, for the purpose of proof of concept, we adopt standard denoising diffusion models as our choice of diffusion model (Ho et al., 2020; Song et al., 2022). We outline the image reconstruction process of a trained DDPM below. Given a test image that possibly contains anomalous regions, a denoising diffusion model is used to generate the corresponding normal image. The reconstruction consists of two processes called *forward process (or diffusion process)* and *reverse process*. In the forward process, noise is sequentially added to the test image so that it converges to a standard Gaussian distribution $\mathcal{N}(\mathbf{0}, I)$. Let $\boldsymbol{x}$ be an image represented as a vector with each element corresponding to a pixel value. Given an original test image $\boldsymbol{x}_0$, noisy images $\boldsymbol{x}_1, \boldsymbol{x}_2, \ldots, \boldsymbol{x}_T$ are sequentially generated, where T is the number of noise addition steps. We consider the distribution of the original and noisy test images, which is denoted by $q(\boldsymbol{x})$, and approximate the distribution by a parametric model $p_\theta(\boldsymbol{x})$ with θ being the parameters. Using a sequence of noise scheduling parameters $0 < \beta_1 < \beta_2 < \cdots < \beta_T < 1$, the forward process is written as

$$q(\boldsymbol{x}_{1:T}|\boldsymbol{x}_0) := \prod_{t=1}^{T} q(\boldsymbol{x}_t|\boldsymbol{x}_{t-1}), \quad \text{where} \quad q(\boldsymbol{x}_t|\boldsymbol{x}_{t-1}) := \mathcal{N}(\sqrt{1-\beta_t}\boldsymbol{x}_{t-1}, \beta_t I).$$

By the reproducibility of the Gaussian distribution, $\boldsymbol{x}_t$ can be rewritten by a linear combination of $\boldsymbol{x}_0$ and ϵ_t, i.e.,

$$\boldsymbol{x}_t = \sqrt{\alpha_t}\boldsymbol{x}_0 + \sqrt{1-\alpha_t}\epsilon_t, \quad \text{with} \quad \epsilon_t \sim \mathcal{N}(\mathbf{0}, I), \tag{1}$$

where $\alpha_t = \prod_{s=1}^{t}(1-\beta_s)$. In the reverse process, a parametric model in the form of $p_\theta(\boldsymbol{x}_{t-1}|\boldsymbol{x}_t) = \mathcal{N}(\mu_\theta(\boldsymbol{x}_t, t), \beta_t I)$ is employed, where $\mu_\theta(\boldsymbol{x}_t, t)$ is obtained by using the predicted noise component $\epsilon_\theta^{(t)}(\boldsymbol{x}_t)$. Typically, a U-Net is used as the model architecture for $\epsilon_\theta^{(t)}(\boldsymbol{x}_t)$. In DDPM (Ho et al., 2020), the loss function for training the noise component is simply written as $||\epsilon_\theta^{(t)}(\boldsymbol{x}_t) - \epsilon_t||_2^2$. Based on (1), given a noisy image $\boldsymbol{x}_t$ after t steps, the reconstruction of the image in the previous step $\boldsymbol{x}_{t-1}$ is obtained as

$$\boldsymbol{x}_{t-1} = \sqrt{\alpha_{t-1}} \cdot f_\theta^{(t)}(\boldsymbol{x}_t) + \sqrt{1-\alpha_{t-1}-\sigma_t^2} \cdot \epsilon_\theta^{(t)}(\boldsymbol{x}_t) + \sigma_t \epsilon_t, \tag{2}$$

where

$$f_\theta^{(t)}(\boldsymbol{x}_t) := (\boldsymbol{x}_t - \sqrt{1-\alpha_t} \cdot \epsilon_\theta^{(t)}(\boldsymbol{x}_t))/\sqrt{\alpha_t}, \tag{3}$$

and

$$\sigma_t = \eta\sqrt{(1-\alpha_{t-1})/(1-\alpha_t)}\sqrt{1-\alpha_t/\alpha_{t-1}}. \tag{4}$$

Here, η is a hyperparameter that controls the randomness in the reverse process. By setting $\eta = 1$, we can create new images by stochastic sampling. On the other hand, if we set $\eta = 0$, deterministic sampling is used for image generation. By recursively sampling as in (2), we can obtain a reconstructed image of the original input $\boldsymbol{x}_0$.

In practice, the reverse process starts from $\boldsymbol{x}_{T'}$ with $T' < T$. Namely, we reconstruct the normal-looking version of the input image not from a completely noisy one, but from one that still contains individual information of the original input image. The smaller T' ensures that the reconstructed image preserves fine details of the input image. Conversely, the larger T' results in the retention of only large-scale features, thereby converting more of the anomalous regions into normal regions (Ho et al., 2020; Mousakhan et al., 2023). The overall reconstruction process of the diffusion model is summarized in Algorithm 1.

Algorithm 1 Reconstruction Process

Require: Input image $\boldsymbol{x}$
1: $\boldsymbol{x}_{T'} \leftarrow \sqrt{\alpha_{T'}}\boldsymbol{x} + \sqrt{1-\alpha_{T'}}\epsilon$
2: **for** $t = T', \ldots, 1$ **do**
3: $\quad f_\theta^{(t)}(\boldsymbol{x}_t) \leftarrow (\boldsymbol{x}_t - \sqrt{1-\alpha_t} \cdot \epsilon_\theta^{(t)}(\boldsymbol{x}_t))/\sqrt{\alpha_t}$
4: $\quad \boldsymbol{x}_{t-1} \leftarrow \sqrt{\alpha_{t-1}} \cdot f_\theta^{(t)}(\boldsymbol{x}_t) + \sqrt{1-\alpha_{t-1}-\sigma_t^2} \cdot \epsilon_\theta^{(t)}(\boldsymbol{x}_t) + \sigma_t\epsilon_t$
5: **end for**
Ensure: Reconstructed image $\boldsymbol{x}_0$

3 Statistical test for diffusion-based anomaly localization

In this section, we formulate the statistical test for detecting anomalous regions by a trained diffusion model. As shown in Figure 1, anomalous region detection by diffusion models is conducted as follows. First, in the training phase, the diffusion model is trained only on normal images. Then, in the test phase, we feed a test image that might contain anomalous regions into the trained diffusion model, and reconstruct it back from a noisy image $\mathbf{x}_{T'}$ at step $T' < T$. By appropriately selecting T', we can generate a normal-looking image that retains individual characteristics of the test input image. If the image does not contain anomalous regions, the reconstructed image is expected to be similar to the original test image. On the other hand, if the image contains anomalous regions, such as tumors, the model may struggle to reconstruct these regions, as it has been trained primarily on normal regions. Therefore, the anomalous regions can be detected by comparing the original test image and its reconstructed one.

Problem formulation We develop a statistical test to quantify the reliability of decision-making based on images generated by diffusion models. To develop a statistical test, we interpret an image as a sum of a true signal component $\boldsymbol{\mu} \in \mathbb{R}^n$ and a noise component $\boldsymbol{\varepsilon} \in \mathbb{R}^n$. We emphasize that the noise component $\boldsymbol{\varepsilon}$ should not be confused with the noise ϵ used in the forward process. No structural assumption is imposed on the signal $\boldsymbol{\mu}$. On the other hand, regarding the noise component, it is assumed to follow a Gaussian distribution, and its covariance matrix is estimated using normal data different from that used for the training of the diffusion model, which is the standard setting of SI. Namely, an image with n pixels can be represented as an n-dimensional random vector,

$$\boldsymbol{X} = (X_1, X_2, \ldots, X_n)^\top = \boldsymbol{\mu} + \boldsymbol{\varepsilon}, \quad \boldsymbol{\varepsilon} \sim \mathcal{N}(\mathbf{0}, \Sigma),$$

where $\boldsymbol{\mu} \in \mathbb{R}^n$ is the unknown true signal vector and Σ is the covariance matrix. In the following, we use $\boldsymbol{X}$ to emphasize that an image is considered as a random vector, while the observed image vector is denoted as $\boldsymbol{x}$.

Let us denote the reconstruction process of the trained diffusion model in Algorithm 1 as the mapping from an input image to the reconstructed image $\mathcal{D}\colon \mathbb{R}^n \ni \boldsymbol{X} \to \mathcal{D}(\boldsymbol{X}) \in \mathbb{R}^n$. The difference between the input image $\boldsymbol{X}$ and the reconstructed image $\mathcal{D}(\boldsymbol{X})$ indicates the reconstruction error. When identifying anomalous regions based on reconstruction error, it is useful to apply some filter to remove the influence of pixel-wise noise. In this study, we use an averaging filter. Let us denote the averaging filter as $\mathcal{F}\colon \mathbb{R}^n \to \mathbb{R}^n$. Then, the process of obtaining the (filtered) reconstruction error is written as

$$\mathcal{E}\colon \mathbb{R}^n \ni \boldsymbol{X} \mapsto |\mathcal{F}(\boldsymbol{X} - \mathcal{D}(\boldsymbol{X}))| \in \mathbb{R}^n,$$

where the absolute value is taken pixel-wise. Anomalous regions are then obtained by applying a threshold to the filtered reconstruction error $\mathcal{E}_i(\boldsymbol{X})$ for each pixel $i \in [n]$. Specifically, we define the anomalous region as the set of pixels whose filtered reconstruction error is greater than a given threshold $\lambda \in \mathbb{R}^+$, i.e.,

$$\mathcal{M}_{\boldsymbol{X}} = \{i \in [n] \mid \mathcal{E}_i(\boldsymbol{X}) \geq \lambda\}. \tag{5}$$

Statistical test for diffusion models In order to quantify the statistical significance of the anomalous regions detected by using the diffusion model, we consider the concrete example of two-sample test. Note that our method can be extended to other statistical tests using various statistics. In the two-sample test, we compare the test image and the randomly chosen reference image in the anomalous region. Let us define an n-dimensional reference input vector,

$$\boldsymbol{X}^{\mathrm{ref}} = (X_1^{\mathrm{ref}}, X_2^{\mathrm{ref}}, \ldots, X_n^{\mathrm{ref}})^\top = \boldsymbol{\mu}^{\mathrm{ref}} + \boldsymbol{\varepsilon}^{\mathrm{ref}}, \text{ with } \boldsymbol{\varepsilon}^{\mathrm{ref}} \sim \mathcal{N}(\mathbf{0}, \Sigma),$$

where $\boldsymbol{\mu}^{\mathrm{ref}} \in \mathbb{R}^n$ is the unknown true signal vector of the reference image, $\boldsymbol{\varepsilon}^{\mathrm{ref}} \in \mathbb{R}^n$ is the noise component, and $\boldsymbol{X}^{\mathrm{ref}}$ is assumed to be independent of $\boldsymbol{X}$. Then, we consider the following null and alternative hypotheses:

$$\mathrm{H}_0\colon \frac{1}{|\mathcal{M}_{\boldsymbol{x}}|}\sum_{i\in\mathcal{M}_{\boldsymbol{x}}} \mu_i = \frac{1}{|\mathcal{M}_{\boldsymbol{x}}|}\sum_{i\in\mathcal{M}_{\boldsymbol{x}}} \mu_i^{\mathrm{ref}} \quad \text{vs.} \quad \mathrm{H}_1\colon \frac{1}{|\mathcal{M}_{\boldsymbol{x}}|}\sum_{i\in\mathcal{M}_{\boldsymbol{x}}} \mu_i \neq \frac{1}{|\mathcal{M}_{\boldsymbol{x}}|}\sum_{i\in\mathcal{M}_{\boldsymbol{x}}} \mu_i^{\mathrm{ref}}, \tag{6}$$

where H_0 is the null hypothesis that the mean pixel values are the same between the test image and the reference image in the observed anomalous region $\mathcal{M}_{\boldsymbol{x}}$, while H_1 is the alternative hypothesis that they are different. A reasonable test statistic for the statistical test in (6) is the difference in mean pixel values between the test image and the reference image in the anomalous region $\mathcal{M}_{\boldsymbol{x}}$, i.e.,

$$T(\boldsymbol{X}, \boldsymbol{X}^{\mathrm{ref}}) = \frac{1}{|\mathcal{M}_{\boldsymbol{x}}|}\sum_{i\in\mathcal{M}_{\boldsymbol{x}}} X_i - \frac{1}{|\mathcal{M}_{\boldsymbol{x}}|}\sum_{i\in\mathcal{M}_{\boldsymbol{x}}} X_i^{\mathrm{ref}} = \boldsymbol{\nu}^\top \begin{pmatrix} \boldsymbol{X} \\ \boldsymbol{X}^{\mathrm{ref}} \end{pmatrix}, \tag{7}$$

where $\boldsymbol{\nu} \in \mathbb{R}^{2n}$ denotes a vector that depends on the anomalous region $\mathcal{M}_{\boldsymbol{x}}$, and hence on $\boldsymbol{x}$ itself, and is defined as

$$\boldsymbol{\nu} = \frac{1}{|\mathcal{M}_{\boldsymbol{x}}|}\begin{pmatrix} \mathbf{1}^n_{\mathcal{M}_{\boldsymbol{x}}} \\ -\mathbf{1}^n_{\mathcal{M}_{\boldsymbol{x}}} \end{pmatrix} \in \mathbb{R}^{2n},$$

where $\mathbf{1}_{\mathcal{C}}^n \in \mathbb{R}^n$ is an n-dimensional vector whose elements are 1 if they belong to the set $\mathcal{C}$ and 0 otherwise. In this case, the p-value is called the naive p-value, and is defined as

$$p_{\text{naive}} = \mathbb{P}_{\text{H}_0}\left(|T(\boldsymbol{X}, \boldsymbol{X}^{\text{ref}})| \geq |T(\boldsymbol{x}, \boldsymbol{x}^{\text{ref}})|\right). \tag{8}$$

If we can identify the sampling distribution of the test statistic $T(\boldsymbol{X}, \boldsymbol{X}^{\text{ref}})$, we can compute a valid p-value that controls the false positive detection rate (i.e., the type I error rate).

4 Selective inference for diffusion-based anomaly localization

In this section, we introduce the SI framework for testing the anomalous regions detected by a diffusion model and propose a method to perform valid hypothesis tests.

4.1 Computing valid p-values via selective inference

Complexity of sampling distribution As mentioned in §3, we need to identify the sampling distribution of the test statistic $T(\boldsymbol{X}, \boldsymbol{X}^{\text{ref}})$ to compute the p-values. If we ignore the fact that the anomalous region is identified by a diffusion model, the test statistic in (7) is simply a linear transformation of the Gaussian random vectors $\boldsymbol{X}$ and $\boldsymbol{X}^{\text{ref}}$, and hence itself follows a Gaussian distribution under the null hypothesis H_0:

$$T(\boldsymbol{X}, \boldsymbol{X}^{\text{ref}}) \sim \mathcal{N}(0, \boldsymbol{\nu}^\top \tilde{\Sigma} \boldsymbol{\nu}), \quad \text{with} \quad \tilde{\Sigma} = \begin{pmatrix} \Sigma & O_n \\ O_n & \Sigma \end{pmatrix},$$

where $\boldsymbol{X}$ and $\boldsymbol{X}^{\text{ref}}$ are assumed to be independent. However, as mentioned in §3, in reality the dependence of $\boldsymbol{\nu}$ on $\boldsymbol{x}$ via the diffusion model is more intricate, making the sampling distribution intractably complex. Consequently, obtaining this sampling distribution directly is challenging.

Selective p-value via conditional sampling distribution Then, we consider the sampling distribution of the test statistic conditional on the event that the anomalous region $\mathcal{M}_{\boldsymbol{X}}$ is the same as the observed anomalous region $\mathcal{M}_{\boldsymbol{x}}$, i.e.,

$$T(\boldsymbol{X}, \boldsymbol{X}^{\text{ref}}) \mid \{\mathcal{M}_{\boldsymbol{X}} = \mathcal{M}_{\boldsymbol{x}}\}.$$

In the context of SI, to make the characterization of the conditional sampling distribution manageable, we also incorporate conditioning on the nuisance parameter that is independent of the test statistic. As a result, the calculation of the conditional sampling distribution in SI can be reduced to a one-dimensional search problem in an n-dimensional data space. The sufficient statistic of the nuisance parameter $\mathcal{Q}_{\boldsymbol{X}, \boldsymbol{X}^{\text{ref}}}$ is written as

$$\mathcal{Q}_{\boldsymbol{X}, \boldsymbol{X}^{\text{ref}}} = \left(I_{2n} - \frac{\tilde{\Sigma}\boldsymbol{\nu}\boldsymbol{\nu}^\top}{\boldsymbol{\nu}^\top \tilde{\Sigma} \boldsymbol{\nu}}\right) \begin{pmatrix} \boldsymbol{X} \\ \boldsymbol{X}^{\text{ref}} \end{pmatrix},$$

where I_{2n} is the identity matrix of size $2n$. By additional conditioning on the nuisance parameter, the selective p-value is defined as

$$p_{\text{selective}} = \mathbb{P}_{\text{H}_0}\left(|T(\boldsymbol{X}, \boldsymbol{X}^{\text{ref}})| \geq |T(\boldsymbol{x}, \boldsymbol{x}^{\text{ref}})| \;\middle|\; \mathcal{M}_{\boldsymbol{X}} = \mathcal{M}_{\boldsymbol{x}}, \mathcal{Q}_{\boldsymbol{X}, \boldsymbol{X}^{\text{ref}}} = \mathcal{Q}_{\boldsymbol{x}, \boldsymbol{x}^{\text{ref}}}\right). \tag{9}$$

The following theorem establishes that the selective p-value is a valid p-value for controlling the false positive detection rate for any significance level $\alpha \in (0, 1)$.

Theorem 4.1. *The selective p-value in* (9) *is valid for controlling the false positive detection rate, i.e,*

$$\mathbb{P}_{\text{H}_0}\left(p_{\text{selective}} \leq \alpha \;\middle|\; \mathcal{M}_{\boldsymbol{X}} = \mathcal{M}_{\boldsymbol{x}}, \mathcal{Q}_{\boldsymbol{X}, \boldsymbol{X}^{\text{ref}}} = \mathcal{Q}_{\boldsymbol{x}, \boldsymbol{x}^{\text{ref}}}\right) = \alpha, \ \forall \alpha \in (0, 1).$$

Then, the selective p-value satisfies the following condition:

$$\mathbb{P}_{\text{H}_0}(p_{\text{selective}} \leq \alpha) = \alpha, \ \forall \alpha \in (0, 1).$$

The proof of Theorem 4.1 is given in Appendix A.1. The following theorem states that the selective p-value can be analytically derived from the conditional sampling distribution, which follows a truncated Gaussian distribution.

Theorem 4.2. *Consider the truncation intervals defined as*

$$\mathcal{Z} = \left\{ z \in \mathbb{R} \;\middle|\; \mathcal{M}_{\boldsymbol{X}(z)} = \mathcal{M}_{\boldsymbol{x}} \right\}, \tag{10}$$

where $\boldsymbol{X}(z)$ *is defined as*

$$\boldsymbol{X}(z) = \boldsymbol{a}_{1:n} + \boldsymbol{b}_{1:n} z, \;\; \textit{where} \;\; \boldsymbol{a} = \mathcal{Q}_{\boldsymbol{x}}, \; \boldsymbol{b} = \frac{\tilde{\Sigma}\boldsymbol{\nu}}{\boldsymbol{\nu}^\top \tilde{\Sigma} \boldsymbol{\nu}}, \tag{11}$$

and $\boldsymbol{a}_{1:n}$ *and* $\boldsymbol{b}_{1:n}$ *denote the first* n *elements of* $\boldsymbol{a}, \boldsymbol{b} \in \mathbb{R}^{2n}$*, respectively. Then, the selective* p*-value in* (9) *can be rewritten as*

$$p_{\text{selective}} = \mathbb{P}_{\text{H}_0}\left(|T(\boldsymbol{X}(Z), \boldsymbol{X}^{\text{ref}}(Z))| \geq |T(\boldsymbol{x}, \boldsymbol{x}^{\text{ref}})| \;\middle|\; Z \in \mathcal{Z} \right). \tag{12}$$

The conditional sampling distribution of the test statistic $T(\boldsymbol{X}(Z), \boldsymbol{X}^{\text{ref}}(Z)) \mid \{Z \in \mathcal{Z}\}$ *follows a truncated Gaussian distribution* $\mathcal{TN}(0, \boldsymbol{\nu}^\top \tilde{\Sigma} \boldsymbol{\nu})$.

The proof of Theorem 4.2 is given in Appendix A.2. Once the truncation intervals $\mathcal{Z}$ are identified, computing the selective p-value in (12) becomes straightforward. Therefore, the remaining task is the identification of $\mathcal{Z}$.

4.2 Identification of truncation intervals $\mathcal{Z}$

Identification of subinterval $\mathcal{Z}^{\text{sub}}$ To tackle the identification of the truncation intervals $\mathcal{Z}$, we employ a divide-and-conquer strategy. Directly characterizing $\mathcal{Z}$ is challenging due to the complexity of the diffusion model's computation. Our method decomposes the n-dimensional data space into a collection of polyhedra by imposing additional conditioning, a process we refer to as *over-conditioning (OC)* (Duy & Takeuchi, 2022). Each polyhedron in the n-dimensional space corresponds to an interval in the one-dimensional space $\mathcal{Z}$. Thus, we can examine these intervals sequentially in $\mathcal{Z}$ to determine whether they yield the same selected anomalous regions as observed. To this end, we need to identify a subinterval $\mathcal{Z}^{\text{sub}} \subseteq \mathcal{Z}$. We show that the anomalous region from a diffusion model can be characterized by a piecewise-linear mapping. Exploiting this property, the subinterval $\mathcal{Z}^{\text{sub}}(\boldsymbol{a} + \boldsymbol{b}z)$ can be computed analytically for each $z \in \mathbb{R}$ by solving a system of linear inequalities (see Appendix B).

Identification of $\mathcal{Z}$ via parametric programming Over-conditioning causes a reduction in power due to excessive conditioning. A technique called *parametric programming* is utilized to explore all intervals along the one-dimensional line, resulting in (10). The truncation intervals $\mathcal{Z}$ can be represented using $\mathcal{Z}^{\text{sub}}$ as

$$\mathcal{Z} = \bigcup_{z \in \mathbb{R} \mid \mathcal{M}_{\boldsymbol{X}(z)} = \mathcal{M}_{\boldsymbol{x}}} \mathcal{Z}^{\text{sub}}(\boldsymbol{a} + \boldsymbol{b}z).$$

Figure 2 illustrates the conditional sampling distribution determined by these truncation intervals. An algorithm for computing the selective p-value is summarized in Algorithm 2.

Algorithm 2 Selective p-value by Parametric Programming

Require: $\boldsymbol{x}, \boldsymbol{x}^{\text{ref}}$
Initialize $\mathcal{Z} \leftarrow \emptyset$
Compute $\mathcal{M}_{\boldsymbol{x}}$, $\boldsymbol{a}$, $\boldsymbol{b}$, and $T(\boldsymbol{x}, \boldsymbol{x}^{\text{ref}})$ by (5), (7), (11)
Initialize z to a sufficiently small value
while z is not large enough **do**
    Compute $\mathcal{Z}^{\text{sub}}(\boldsymbol{a} + \boldsymbol{b}z)$ and $\mathcal{M}_{\boldsymbol{X}(z)}$ by (13)
    if $\mathcal{M}_{\boldsymbol{X}(z)} = \mathcal{M}_{\boldsymbol{x}}$ **then**
        $\mathcal{Z} \leftarrow \mathcal{Z} \cup \mathcal{Z}^{\text{sub}}(\boldsymbol{a} + \boldsymbol{b}z)$
    end if
    $z \leftarrow \max \mathcal{Z}^{\text{sub}}(\boldsymbol{a} + \boldsymbol{b}z) + \gamma$, where $0 < \gamma \ll 1$
end while
$p_{\text{selective}} = \mathbb{P}_{\text{H}_0}\left(|T(\boldsymbol{X}(Z), \boldsymbol{X}^{\text{ref}}(Z))| \geq |T(\boldsymbol{x}, \boldsymbol{x}^{\text{ref}})| \;\middle|\; Z \in \mathcal{Z} \right)$
Ensure: $p_{\text{selective}}$

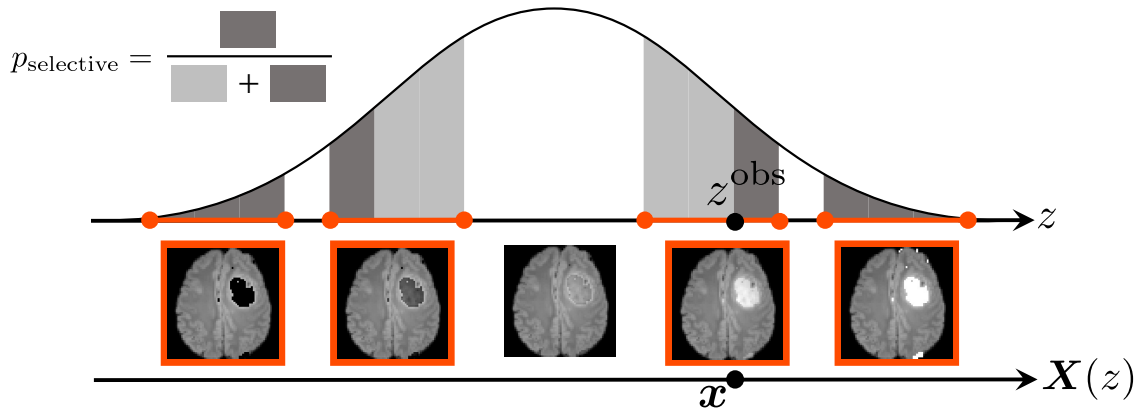

Figure 2: Schematic illustration of the selective inference procedure for diffusion models. It shows how the image $\boldsymbol{X}(z)$ changes with z. The truncation intervals that yield the same anomalous region $\mathcal{M}_{\boldsymbol{X}(z)}$ as the observed anomalous region $\mathcal{M}_{\boldsymbol{x}}$ define the conditional sampling distribution. The $p_{\text{selective}}$ denotes the proportion of probability mass within the truncation intervals.

5 Experiments

We compared our proposed method (`proposed`) on type I error rate and power with the following methods (see Appendix C for details of those methods):

- `w/o-pp`: An ablation study without the parametric programming technique described in §4.2. The p-value is computed using (12), with $\mathcal{Z}$ replaced by $\mathcal{Z}^{\text{sub}}(\boldsymbol{a} + \boldsymbol{b}z^{\text{obs}})$.
- `naive`: This method is conventionally used in practice. The p-value is computed as (8).
- `bonferroni`: This method uses the Bonferroni correction. Bonferroni correction is widely used for multiple testing correction.
- `permutation`: This method uses the permutation test. A permutation test is widely used for non-parametric hypothesis testing.

The architecture of diffusion models used in all experiments is detailed in Appendix D. We executed all experiments on AMD EPYC 9474F processor, 48-core 3.6GHz CPU and 768GB memory.

5.1 Numerical experiments

Experimental setup Experiments on the type I error rate and power were conducted with two types of covariance matrices: independent $\Sigma = I_n \in \mathbb{R}^{n \times n}$ and correlation $\Sigma = (0.5^{|i-j|})_{ij} \in \mathbb{R}^{n \times n}$. In the type I error rate experiments, we used only normal images. The synthetic dataset for normal images is generated to follow $\boldsymbol{X} \sim \mathcal{N}(\boldsymbol{0}, \Sigma)$. We generated 1,000 normal images for $n \in \{64, 256, 1024, 4096\}$. In the power experiments, we used only abnormal images. We generated 1,000 abnormal images $\boldsymbol{X} \sim \mathcal{N}(\boldsymbol{\mu}, \Sigma)$. The mean vector $\boldsymbol{\mu}$ is defined as $\mu_i = \Delta$ for all $i \in \mathcal{S}$, and $\mu_i = 0$ for all $i \in [n] \backslash \mathcal{S}$, where $\mathcal{S} \subset [n]$ is the anomalous region with its position randomly chosen. The image size of the abnormal images was set to 4096, with signals $\Delta \in \{1, 2, 3, 4\}$. In all experiments, we generated the synthetic dataset for 1,000 reference images to follow $\boldsymbol{X}^{\text{ref}} \sim \mathcal{N}(\boldsymbol{0}, \Sigma)$. The threshold was set to $\lambda = 0.8$, and the kernel size of the averaging filter was set to 3. All experiments were conducted under the significance level $\alpha = 0.05$. The diffusion models were trained on the normal images from the synthetic dataset. The diffusion models were trained with $T = 1000$ and the initial time step of the reverse process was set to $T' = 460$, and the reconstruction was performed using 5-step sampling (see Appendix E for details). The noise schedule $\beta_1, \beta_2, \ldots, \beta_T$ was set to linear. In all experiments, we generated normal-looking images through probabilistic sampling, with η set to 1.

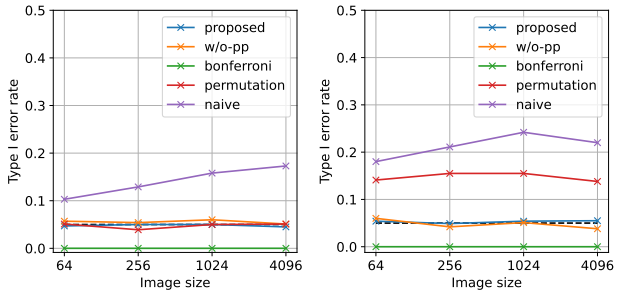

(a) Independence (b) Correlation

Figure 3: Type I error rate comparison

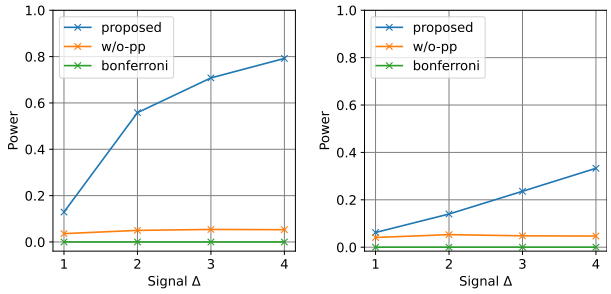

(a) Independence (b) Correlation

Figure 4: Power comparison

Table 1: Type I error rate and power comparison on real-world datasets at the significance level of $\alpha(= 0.05)$. The `proposed` and `bonferroni` methods control the type I error rate at or below α for each dataset, whereas `naive` fails to do so and is therefore unreliable. Additionally, `proposed` achieves higher power than `bonferroni`. Figure 5 shows qualitative results of the `proposed` and `naive` methods on the MVTec AD dataset and the BraTS dataset.

	`naive`		`bonferroni`		`proposed`	
Dataset	Type I Error	Power	Type I Error	Power	Type I Error	Power
Bottle	0.46	N.A	0.00	0.00	**0.04**	**0.18**
Cable	0.88	N.A	0.00	0.00	**0.02**	**0.40**
Grid	0.82	N.A	0.00	0.00	**0.06**	**0.34**
Transistor	0.86	N.A	0.00	0.00	**0.08**	**0.28**
BraTS (T2-FLAIR)	0.59	N.A	0.00	0.00	**0.05**	**0.28**

Results Figure 3 shows the comparison results of type I error rates. The proposed methods `proposed` and `w/o-pp` can control the type I error rate at the significance level α, and `bonferroni` can control the type I error rate below the significance level α. In contrast, `naive` and `permutation` cannot control the type I error rate. Figure 4 shows the comparison results of powers. Since `naive` and `permutation` cannot control the type I error rate, their powers are not considered. Among the methods that can control the type I error rate, the `proposed` has the highest power. The ablation study `w/o-pp` is over-conditioned and `bonferroni` is conservative because there are many hypotheses, so they have low power.

5.2 Real-world data experiments

Experimental setup We conducted experiments using T2-FLAIR MRI brain scans from the Brain Tumor Segmentation (BraTS) 2023 dataset (Karargyris et al., 2023; LaBella et al., 2023) and MVTec AD dataset (Bergmann et al., 2019). The details of the experimental settings are described in Appendix F.

Results Table 1 shows the comparison of the type I error rate and power. The `naive` cannot control the type I error rate, while the `proposed` and `bonferroni` can control the type I error rate below the significance level α. The `proposed` has higher power than `bonferroni`.

6 Conclusions

We introduced the DAL-Test, a novel statistical procedure for anomaly localization identified by a diffusion model. With the proposed DAL-Test, the false positive detection rate can be controlled at the significance level because statistical inference is conducted conditional on the fact that the anomalous regions are identified by using a diffusion model. We demonstrated that the DAL-Test has higher power than the Bonferroni correction, the only existing method for controlling the false positive detection rate.

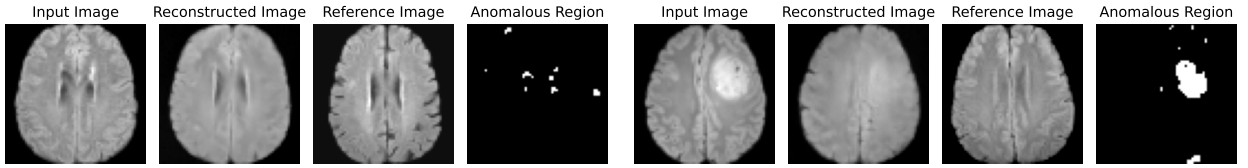

p_{naive} : 0.031, $p_{\text{selective}}$: 0.331 p_{naive} : 0.000, $p_{\text{selective}}$: 0.003

(a) Brain MRI (Left: Normal, Right: Anomaly)

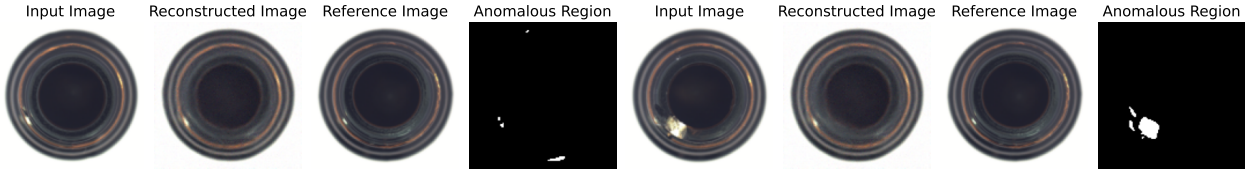

p_{naive} : 0.000, $p_{\text{selective}}$: 0.907 p_{naive} : 0.000, $p_{\text{selective}}$: 0.010

(b) Bottle (Left: Normal, Right: Anomaly)

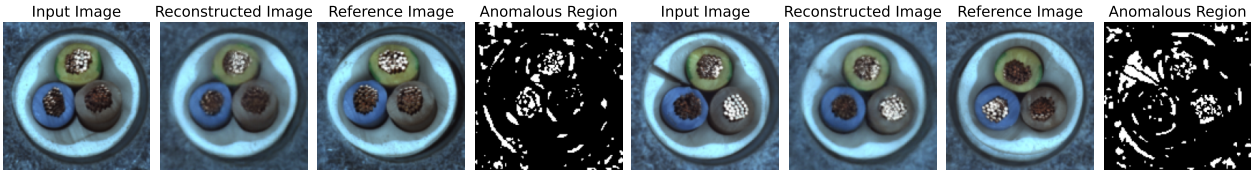

p_{naive} : 0.000, $p_{\text{selective}}$: 0.567 p_{naive} : 0.000, $p_{\text{selective}}$: 0.000

(c) Cable (Left: Normal, Right: Anomaly)

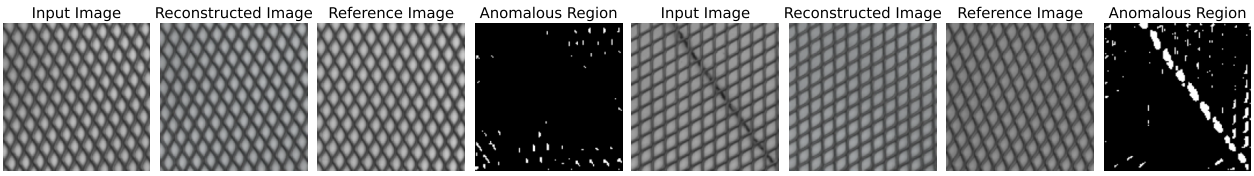

p_{naive} : 0.028, $p_{\text{selective}}$: 0.789 p_{naive} : 0.000, $p_{\text{selective}}$: 0.018

(d) Grid (Left: Normal, Right: Anomaly)

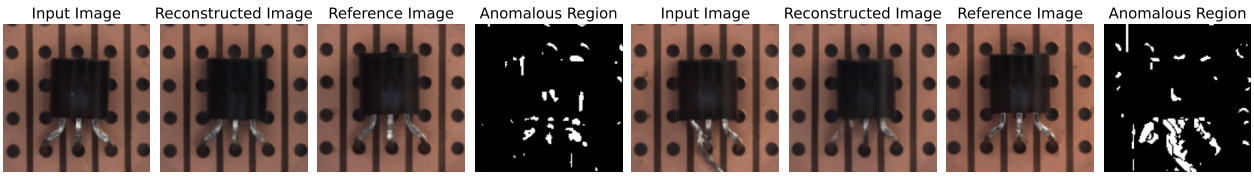

p_{naive} : 0.000, $p_{\text{selective}}$: 0.769 p_{naive} : 0.000, $p_{\text{selective}}$: 0.018

(e) Transistor (Left: Normal, Right: Anomaly)

Figure 5: Results of the `proposed` and `naive` methods on the BraTS dataset (one example) and the MVTec AD dataset (four categories). For each dataset, the left image is a normal sample and the right image is an anomalous sample. The $p_{\text{selective}}$ is high for normal images (true negative) and low for anomalous images (true positive), demonstrating that the proposed method correctly controls the false positive detection rate. In contrast, the p_{naive} remains low for both normal and anomalous images, indicating an inflated false positive rate.

References

Christoph Baur, Stefan Denner, Benedikt Wiestler, Nassir Navab, and Shadi Albarqouni. Autoencoders for unsupervised anomaly segmentation in brain mr images: A comparative study. *Medical Image Analysis*,

69:101952, 2021. ISSN 1361-8415. doi: https://doi.org/10.1016/j.media.2020.101952. URL https://www.sciencedirect.com/science/article/pii/S1361841520303169.

Paul Bergmann, Michael Fauser, David Sattlegger, and Carsten Steger. Mvtec ad — a comprehensive real-world dataset for unsupervised anomaly detection. In *2019 IEEE/CVF Conference on Computer Vision and Pattern Recognition (CVPR)*, pp. 9584–9592, 2019. doi: 10.1109/CVPR.2019.00982.

Shuxiao Chen and Jacob Bien. Valid inference corrected for outlier removal. *Journal of Computational and Graphical Statistics*, 29(2):323–334, 2020.

Xiaoran Chen and Ender Konukoglu. Unsupervised detection of lesions in brain MRI using constrained adversarial auto-encoders. In *Medical Imaging with Deep Learning*, 2018. URL https://openreview.net/forum?id=H1nGLZ2oG.

Jun Kang Chow, Zhaoyu Su, Jimmy Wu, Pin Siang Tan, Xin Mao, and Yu-Hsing Wang. Anomaly detection of defects on concrete structures with the convolutional autoencoder. *Advanced Engineering Informatics*, 45:101105, 2020.

Diptesh Das, Vo Nguyen Le Duy, Hiroyuki Hanada, Koji Tsuda, and Ichiro Takeuchi. Fast and more powerful selective inference for sparse high-order interaction model. *arXiv preprint arXiv:2106.04929*, 2021.

Vo Nguyen Le Duy and Ichiro Takeuchi. More powerful conditional selective inference for generalized lasso by parametric programming. *The Journal of Machine Learning Research*, 23(1):13544–13580, 2022.

Vo Nguyen Le Duy, Hiroki Toda, Ryota Sugiyama, and Ichiro Takeuchi. Computing valid p-value for optimal changepoint by selective inference using dynamic programming. In *Advances in Neural Information Processing Systems*, 2020.

Vo Nguyen Le Duy, Shogo Iwazaki, and Ichiro Takeuchi. Quantifying statistical significance of neural network-based image segmentation by selective inference. *Advances in Neural Information Processing Systems*, 35: 31627–31639, 2022.

William Fithian, Dennis Sun, and Jonathan Taylor. Optimal inference after model selection. *arXiv preprint arXiv:1410.2597*, 2014.

Alessandro Fontanella, Grant Mair, Joanna Wardlaw, Emanuele Trucco, and Amos Storkey. Diffusion models for counterfactual generation and anomaly detection in brain images. *IEEE Transactions on Medical Imaging*, 2024.

Lucy L Gao, Jacob Bien, and Daniela Witten. Selective inference for hierarchical clustering. *Journal of the American Statistical Association*, pp. 1–11, 2022.

Jonathan Ho, Ajay Jain, and Pieter Abbeel. Denoising diffusion probabilistic models. In H. Larochelle, M. Ranzato, R. Hadsell, M.F. Balcan, and H. Lin (eds.), *Advances in Neural Information Processing Systems*, volume 33, pp. 6840–6851. Curran Associates, Inc., 2020. URL https://proceedings.neurips.cc/paper_files/paper/2020/file/4c5bcfec8584af0d967f1ab10179ca4b-Paper.pdf.

Sangwon Hyun, Max G'sell, and Ryan J Tibshirani. Exact post-selection inference for the generalized lasso path. *Electronic Journal of Statistics*, 12(1):1053–1097, 2018.

Hasan Iqbal, Umar Khalid, Chen Chen, and Jing Hua. Unsupervised anomaly detection in medical images using masked diffusion model. In *International Workshop on Machine Learning in Medical Imaging*, pp. 372–381. Springer, 2023.

Debasish Jana, Jayant Patil, Sudheendra Herkal, Satish Nagarajaiah, and Leonardo Duenas-Osorio. Cnn and convolutional autoencoder (cae) based real-time sensor fault detection, localization, and correction. *Mechanical Systems and Signal Processing*, 169:108723, 2022.

Sean Jewell, Paul Fearnhead, and Daniela Witten. Testing for a change in mean after changepoint detection. *Journal of the Royal Statistical Society Series B: Statistical Methodology*, 84(4):1082–1104, 2022.

Alexandros Karargyris, Renato Umeton, Micah J. Sheller, Alejandro Aristizabal, Johnu George, Anna Wuest, Sarthak Pati, Hasan Kassem, Maximilian Zenk, Ujjwal Baid, Prakash Narayana Moorthy, Alexander Chowdhury, Junyi Guo, Sahil Nalawade, Jacob Rosenthal, David Kanter, Maria Xenochristou, Daniel J. Beutel, Verena Chung, Timothy Bergquist, James Eddy, Abubakar Abid, Lewis Tunstall, Omar Sanseviero, Dimitrios Dimitriadis, Yiming Qian, Xinxing Xu, Yong Liu, Rick Siow Mong Goh, Srini Bala, Victor Bittorf, Sreekar Reddy Puchala, Biagio Ricciuti, Soujanya Samineni, Eshna Sengupta, Akshay Chaudhari, Cody Coleman, Bala Desinghu, Gregory Diamos, Debo Dutta, Diane Feddema, Grigori Fursin, Xinyuan Huang, Satyananda Kashyap, Nicholas Lane, Indranil Mallick, Pietro Mascagni, Virendra Mehta, Cassiano Ferro Moraes, Vivek Natarajan, Nikola Nikolov, Nicolas Padoy, Gennady Pekhimenko, Vijay Janapa Reddi, G. Anthony Reina, Pablo Ribalta, Abhishek Singh, Jayaraman J. Thiagarajan, Jacob Albrecht, Thomas Wolf, Geralyn Miller, Huazhu Fu, Prashant Shah, Daguang Xu, Poonam Yadav, David Talby, Mark M. Awad, Jeremy P. Howard, Michael Rosenthal, Luigi Marchionni, Massimo Loda, Jason M. Johnson, Spyridon Bakas, Peter Mattson, FeTS Consortium, BraTS-2020 Consortium, and AI4SafeChole Consortium. Federated benchmarking of medical artificial intelligence with medperf. *Nature Machine Intelligence*, 5(7):799–810, July 2023. doi: 10.1038/s42256-023-00652-2. URL `https://doi.org/10.1038/s42256-023-00652-2`.

Dominic LaBella, Maruf Adewole, Michelle Alonso-Basanta, Talissa Altes, Syed Muhammad Anwar, Ujjwal Baid, Timothy Bergquist, Radhika Bhalerao, Sully Chen, Verena Chung, Gian-Marco Conte, Farouk Dako, James Eddy, Ivan Ezhov, Devon Godfrey, Fathi Hilal, Ariana Familiar, Keyvan Farahani, Juan Eugenio Iglesias, Zhifan Jiang, Elaine Johanson, Anahita Fathi Kazerooni, Collin Kent, John Kirkpatrick, Florian Kofler, Koen Van Leemput, Hongwei Bran Li, Xinyang Liu, Aria Mahtabfar, Shan McBurney-Lin, Ryan McLean, Zeke Meier, Ahmed W Moawad, John Mongan, Pierre Nedelec, Maxence Pajot, Marie Piraud, Arif Rashid, Zachary Reitman, Russell Takeshi Shinohara, Yury Velichko, Chunhao Wang, Pranav Warman, Walter Wiggins, Mariam Aboian, Jake Albrecht, Udunna Anazodo, Spyridon Bakas, Adam Flanders, Anastasia Janas, Goldey Khanna, Marius George Linguraru, Bjoern Menze, Ayman Nada, Andreas M Rauschecker, Jeff Rudie, Nourel Hoda Tahon, Javier Villanueva-Meyer, Benedikt Wiestler, and Evan Calabrese. The asnr-miccai brain tumor segmentation (brats) challenge 2023: Intracranial meningioma, 2023. URL `https://arxiv.org/abs/2305.07642`.

Vo Nguyen Le Duy, Hsuan-Tien Lin, and Ichiro Takeuchi. Cad-da: Controllable anomaly detection after domain adaptation by statistical inference. In *International Conference on Artificial Intelligence and Statistics*, pp. 1828–1836. PMLR, 2024.

Jason D Lee and Jonathan E Taylor. Exact post model selection inference for marginal screening. *Advances in neural information processing systems*, 27, 2014.

Jason D Lee, Yuekai Sun, and Jonathan E Taylor. Evaluating the statistical significance of biclusters. *Advances in neural information processing systems*, 28, 2015.

Jason D Lee, Dennis L Sun, Yuekai Sun, and Jonathan E Taylor. Exact post-selection inference, with application to the lasso. *The Annals of Statistics*, 44(3):907–927, 2016.

Jinpeng Li, Hanqun Cao, Jiaze Wang, Furui Liu, Qi Dou, Guangyong Chen, and Pheng-Ann Heng. Fast non-markovian diffusion model for weakly supervised anomaly detection in brain mr images. In *International Conference on Medical Image Computing and Computer-Assisted Intervention*, pp. 579–589. Springer, 2023.

Fanbin Lu, Xufeng Yao, Chi-Wing Fu, and Jiaya Jia. Removing anomalies as noises for industrial defect localization. In *Proceedings of the IEEE/CVF International Conference on Computer Vision*, pp. 16166–16175, 2023.

Daiki Miwa, Duy Vo Nguyen Le, and Ichiro Takeuchi. Valid p-value for deep learning-driven salient region. In *Proceedings of the 11th International Conference on Learning Representation*, 2023.

Daiki Miwa, Tomohiro Shiraishi, Vo Nguyen Le Duy, Teruyuki Katsuoka, and Ichiro Takeuchi. Statistical test for anomaly detections by variational auto-encoders. *arXiv preprint arXiv:2402.03724*, 2024.

Arian Mousakhan, Thomas Brox, and Jawad Tayyub. Anomaly detection with conditioned denoising diffusion models, 2023.

Walter HL Pinaya, Mark S Graham, Robert Gray, Pedro F Da Costa, Petru-Daniel Tudosiu, Paul Wright, Yee H Mah, Andrew D MacKinnon, James T Teo, Rolf Jager, et al. Fast unsupervised brain anomaly detection and segmentation with diffusion models. In *International Conference on Medical Image Computing and Computer-Assisted Intervention*, pp. 705–714. Springer, 2022.

David Rügamer and Sonja Greven. Inference for l 2-boosting. *Statistics and computing*, 30(2):279–289, 2020.

Xinyu Sheng, Shande Tuo, and Lu Wang. Surface anomaly detection and localization with diffusion-based reconstruction. In *2024 International Joint Conference on Neural Networks (IJCNN)*, pp. 1–8. IEEE, 2024.

Tomohiro Shiraishi, Daiki Miwa, Teruyuki Katsuoka, Vo Nguyen Le Duy, Koichi Taji, and Ichiro Takeuchi. Statistical test for attention map in vision transformers. *International Conference on Machine Learning*, 2024.

Jiaming Song, Chenlin Meng, and Stefano Ermon. Denoising diffusion implicit models, 2022.

Shinya Suzumura, Kazuya Nakagawa, Yuta Umezu, Koji Tsuda, and Ichiro Takeuchi. Selective inference for sparse high-order interaction models. In *Proceedings of the 34th International Conference on Machine Learning-Volume 70*, pp. 3338–3347. JMLR. org, 2017.

Kosuke Tanizaki, Noriaki Hashimoto, Yu Inatsu, Hidekata Hontani, and Ichiro Takeuchi. Computing valid p-values for image segmentation by selective inference. In *Proceedings of the IEEE/CVF Conference on Computer Vision and Pattern Recognition*, pp. 9553–9562, 2020.

Jonathan Taylor and Robert J Tibshirani. Statistical learning and selective inference. *Proceedings of the National Academy of Sciences*, 112(25):7629–7634, 2015.

Justin Tebbe and Jawad Tayyub. Dynamic addition of noise in a diffusion model for anomaly detection. In *Proceedings of the IEEE/CVF Conference on Computer Vision and Pattern Recognition*, pp. 3940–3949, 2024.

Ryan J Tibshirani, Jonathan Taylor, Richard Lockhart, and Robert Tibshirani. Exact post-selection inference for sequential regression procedures. *Journal of the American Statistical Association*, 111(514):600–620, 2016.

Toshiaki Tsukurimichi, Yu Inatsu, Vo Nguyen Le Duy, and Ichiro Takeuchi. Conditional selective inference for robust regression and outlier detection using piecewise-linear homotopy continuation. *arXiv preprint arXiv:2104.10840*, 2021.

Julian Wyatt, Adam Leach, Sebastian M. Schmon, and Chris G. Willcocks. Anoddpm: Anomaly detection with denoising diffusion probabilistic models using simplex noise. In *Proceedings of the IEEE/CVF Conference on Computer Vision and Pattern Recognition (CVPR) Workshops*, pp. 650–656, June 2022.

Fan Yang, Rina Foygel Barber, Prateek Jain, and John Lafferty. Selective inference for group-sparse linear models. In *Advances in Neural Information Processing Systems*, pp. 2469–2477, 2016.

Xinyi Zhang, Naiqi Li, Jiawei Li, Tao Dai, Yong Jiang, and Shu-Tao Xia. Unsupervised surface anomaly detection with diffusion probabilistic model. In *Proceedings of the IEEE/CVF International Conference on Computer Vision*, pp. 6782–6791, 2023.

A Proofs

A.1 Proof of Theorem 4.1

Under the null hypothesis, the probability integral transform implies that

$$p_{\text{selective}} \mid \left\{\mathcal{M}_{\boldsymbol{X}} = \mathcal{M}_{\boldsymbol{x}}, \mathcal{Q}_{\boldsymbol{X},\boldsymbol{X}^{\text{ref}}} = \mathcal{Q}_{\boldsymbol{x},\boldsymbol{x}^{\text{ref}}}\right\} \sim \text{Uniform}(0,1),$$

and hence for any $\alpha \in (0,1)$,

$$\mathbb{P}\left(p_{\text{selective}} \leq \alpha \mid \left\{\mathcal{M}_{\boldsymbol{X}} = \mathcal{M}_{\boldsymbol{x}}, \mathcal{Q}_{\boldsymbol{X},\boldsymbol{X}^{\text{ref}}} = \mathcal{Q}_{\boldsymbol{x},\boldsymbol{x}^{\text{ref}}}\right\}\right) = \alpha,\ \forall \alpha \in (0,1).$$

By marginalizing over the nuisance parameter $\mathcal{Q}_{\boldsymbol{x}}$, we have

$$\begin{aligned}
&\mathbb{P}\left(p_{\text{selective}} \leq \alpha \mid \mathcal{M}_{\boldsymbol{X}} = \mathcal{M}_{\boldsymbol{x}}, \mathcal{Q}_{\boldsymbol{X},\boldsymbol{X}^{\text{ref}}} = \mathcal{Q}_{\boldsymbol{x},\boldsymbol{x}^{\text{ref}}}\right) \\
&= \int_{\mathbb{R}^n} \mathbb{P}_{\text{H}_0}(p_{\text{selective}} \leq \alpha \mid \mathcal{M}_{\boldsymbol{X}} = \mathcal{M}_{\boldsymbol{x}}, \mathcal{Q}_{\boldsymbol{X},\boldsymbol{X}^{\text{ref}}} = \mathcal{Q}_{\boldsymbol{x},\boldsymbol{x}^{\text{ref}}})\ \mathbb{P}_{\text{H}_0}(\mathcal{Q}_{\boldsymbol{X},\boldsymbol{X}^{\text{ref}}} = \mathcal{Q}_{\boldsymbol{x},\boldsymbol{x}^{\text{ref}}} \mid \mathcal{M}_{\boldsymbol{X}} = \mathcal{M}_{\boldsymbol{x}}) d\mathcal{Q}_{\boldsymbol{x}} \\
&= \alpha \int_{\mathbb{R}^n} \mathbb{P}_{\text{H}_0}(\mathcal{Q}_{\boldsymbol{X},\boldsymbol{X}^{\text{ref}}} = \mathcal{Q}_{\boldsymbol{x},\boldsymbol{x}^{\text{ref}}} \mid \mathcal{M}_{\boldsymbol{X}} = \mathcal{M}_{\boldsymbol{x}}) d\mathcal{Q}_{\boldsymbol{x}}. \\
&= \alpha
\end{aligned}$$

Therefore, we have

$$\begin{aligned}
&\mathbb{P}_{\text{H}_0}\left(p_{\text{selective}} \leq \alpha\right) \\
&= \sum_{\mathcal{M}_{\boldsymbol{x}} \in 2^{[n]}} \mathbb{P}_{\text{H}_0}(\mathcal{M}_{\boldsymbol{x}})\ \mathbb{P}_{\text{H}_0}(p_{\text{selective}} \leq \alpha \mid \mathcal{M}_{\boldsymbol{X}} = \mathcal{M}_{\boldsymbol{x}}) \\
&= \alpha \sum_{\mathcal{M}_{\boldsymbol{x}} \in 2^{[n]}} \mathbb{P}_{\text{H}_0}(\mathcal{M}_{\boldsymbol{x}}) \\
&= \alpha
\end{aligned}$$

A.2 Proof of Theorem 4.2

The conditioning on $\mathcal{Q}_{\boldsymbol{X},\boldsymbol{X}^{\text{ref}}} = \mathcal{Q}_{\boldsymbol{x},\boldsymbol{x}^{\text{ref}}}$ implies

$$\mathcal{Q}_{\boldsymbol{X},\boldsymbol{X}^{\text{ref}}} = \mathcal{Q}_{\boldsymbol{x},\boldsymbol{x}^{\text{ref}}} \Leftrightarrow \left(I_{2n} - \frac{\tilde{\Sigma}\boldsymbol{\nu}\boldsymbol{\nu}^\top}{\boldsymbol{\nu}^\top\tilde{\Sigma}\boldsymbol{\nu}}\right)\begin{pmatrix}\boldsymbol{X}\\ \boldsymbol{X}^{\text{ref}}\end{pmatrix} = \mathcal{Q}_{\boldsymbol{x},\boldsymbol{x}^{\text{ref}}} \Leftrightarrow \begin{pmatrix}\boldsymbol{X}\\ \boldsymbol{X}^{\text{ref}}\end{pmatrix} = \boldsymbol{a} + \boldsymbol{b}z,$$

where $z = T(\boldsymbol{X}, \boldsymbol{X}^{\text{ref}}) \in \mathbb{R}$. Hence,

$$\begin{aligned}
&\left\{\begin{pmatrix}\boldsymbol{X}\\ \boldsymbol{X}^{\text{ref}}\end{pmatrix} \middle| \mathcal{M}_{\boldsymbol{X}} = \mathcal{M}_{\boldsymbol{x}}, \mathcal{Q}_{\boldsymbol{X},\boldsymbol{X}^{\text{ref}}} = \mathcal{Q}_{\boldsymbol{x},\boldsymbol{x}^{\text{ref}}}\right\} \\
&= \left\{\begin{pmatrix}\boldsymbol{X}\\ \boldsymbol{X}^{\text{ref}}\end{pmatrix} \middle| \mathcal{M}_{\boldsymbol{X}} = \mathcal{M}_{\boldsymbol{x}}, \begin{pmatrix}\boldsymbol{X}\\ \boldsymbol{X}^{\text{ref}}\end{pmatrix} = \boldsymbol{a} + \boldsymbol{b}z\right\} \\
&= \left\{\begin{pmatrix}\boldsymbol{X}\\ \boldsymbol{X}^{\text{ref}}\end{pmatrix} \middle| \mathcal{M}_{\boldsymbol{X}(z)} = \mathcal{M}_{\boldsymbol{x}}\right\} \\
&= \left\{\boldsymbol{a} + \boldsymbol{b}z \mid z \in \mathcal{Z}\right\},
\end{aligned}$$

where $\boldsymbol{X}(z) = \boldsymbol{a}_{1:n} + \boldsymbol{b}_{1:n}z$. As a result,

$$T(\boldsymbol{X}, \boldsymbol{X}^{\text{ref}}) \mid \left\{\mathcal{M}_{\boldsymbol{X}} = \mathcal{M}_{\boldsymbol{x}}, \mathcal{Q}_{\boldsymbol{X},\boldsymbol{X}^{\text{ref}}} = \mathcal{Q}_{\boldsymbol{x},\boldsymbol{x}^{\text{ref}}}\right\} \sim \mathcal{TN}(0, \boldsymbol{\nu}^\top\tilde{\Sigma}\boldsymbol{\nu})$$

B Calculating the subinterval $\mathcal{Z}^{\text{sub}}$ for diffusion models

We show that a reconstruction error $\mathcal{E}$ via diffusion models can be expressed as a piecewise-linear function of $\boldsymbol{X}$. To show this, we see that both the forward process and reverse process of the diffusion model are

piecewise-linear functions as long as we employ a class of U-Net described below. It is easy to see the piecewise-linearity of the forward process as long as we fix the random seed for ϵ_t. To make the reverse process a piecewise-linear function, we employ a U-Net composed of piecewise-linear components such as ReLU activation functions and pooling layers. Then, $\epsilon_\theta^{(t)}(\mathbf{x}_t)$ is represented as a piecewise-linear function of $\mathbf{x}_t$. Moreover, since $f_\theta^{(t)}(\mathbf{x}_t)$ in (3) is a composite function of $\epsilon_\theta^{(t)}(\mathbf{x}_t)$, it is also a piecewise-linear function. By combining them together, we see that $\mathbf{x}_{t-1}$ is written as a piecewise-linear function of $\mathbf{x}_t$. Therefore, the entire reconstruction process is a piecewise-linear function since it just repeats the above operation multiple times (see Algorithm 1). As a result, the entire mapping $\mathcal{D}(\mathbf{X})$ of the diffusion model is a piecewise-linear function of the input image $\boldsymbol{X}$. Moreover, since the averaging filter $\mathcal{F}$ and the absolute operation are also piecewise-linear functions, $|\mathcal{F}(\boldsymbol{X} - \mathcal{D}(\boldsymbol{X}))|(= \mathcal{E}(\boldsymbol{X}))$ is piecewise-linear. Exploiting this piecewise-linearity, the interval $\mathcal{Z}^{\mathrm{sub}}$ can be computed. The following theorem states that the subinterval $\mathcal{Z}^{\mathrm{sub}}(\boldsymbol{a} + \boldsymbol{b}z)$ can be computed by solving a set of linear inequalities.

Theorem B.1. *The piecewise-linear mapping $\mathcal{A}(\boldsymbol{X})$ can be expressed as a linear function of the input image $\boldsymbol{X}$ on each polyhedral region $\mathcal{P}_k$.*

$$\forall \boldsymbol{X} \in \mathcal{P}^{(k)}, \;\; \mathcal{A}(\boldsymbol{X}) = \boldsymbol{\delta}^{(k)} + \boldsymbol{\Delta}^{(k)} \boldsymbol{X},$$

where $\boldsymbol{\delta}^{(k)}$ and $\boldsymbol{\Delta}^{(k)}$ for $k \in [K]$ are the constant vector and the coefficient matrix with appropriate dimensions for the k-th polyhedron, respectively. Using the notation in (12)*, since the input image $\boldsymbol{X}(z)$ is restricted on a one-dimensional line, each component of the output of $\mathcal{A}$ is written as*

$$\forall z \in [L_i^{(k')}, U_i^{(k')}], \;\; \mathcal{A}_i(\boldsymbol{X}(z)) = \kappa_i^{(k')} + \rho_i^{(k')} z,$$

where $\kappa_i^{(k')} \in \mathbb{R}$ and $\rho_i^{(k')} \in \mathbb{R}$ for $k' \in [K_i^{'}]$ are the coefficient and the constant of the k'-th interval $[L_i^{(k')}, U_i^{(k')}]$, and $K_i^{'}$ is the number of linear pieces of $\mathcal{A}_i$. For each $i \in [n]$, there exists $k' \in [K_i^{'}]$ such that $z \in [L_i^{(k')}, U_i^{(k')}]$, then the inequality $\mathcal{A}_i(\boldsymbol{X}(z)) \geq \lambda$, can be solved as

$$[L_i(z), U_i(z)] \coloneqq \begin{cases} \left[\max\left(L_i^{(k')}, (\lambda - \rho_i^{(k')})/\kappa_i^{(k')}\right), U_i^{(k')}\right] & \text{if } \kappa_i^{(k')} > 0, \\ \left[L_i^{(k')}, \min\left(U_i^{(k')}, (\lambda - \rho_i^{(k')})/\kappa_i^{(k')}\right)\right] & \text{if } \kappa_i^{(k')} < 0. \end{cases}$$

By applying the above theorem, we denote the subinterval as

$$\mathcal{Z}^{\mathrm{sub}}(\boldsymbol{a} + \boldsymbol{b}z) = \bigcap_{i \in [n]} [L_i(z), U_i(z)]. \tag{13}$$

C Comparison methods for numerical experiments

We compared our proposed method with the following methods:

- `proposed`: The proposed method uses parametric programming.
- `w/o-pp`: The proposed method uses over-conditioning (without parametric programming). The p-value is calculated as

$$p_{\mathrm{ablation}} = \mathbb{P}_{\mathrm{H}_0}\left(|T(\boldsymbol{X}(Z), \boldsymbol{X}^{\mathrm{ref}}(Z))| > |T(\boldsymbol{x}, \boldsymbol{x}^{\mathrm{ref}})| \;\middle|\; Z \in \mathcal{Z}^{\mathrm{sub}}(\boldsymbol{a} + \boldsymbol{b}z^{\mathrm{obs}})\right)$$

- `naive`: The naive method. This method uses a conventional z-test without any conditioning in (8).
- `bonferroni`: To control the type I error rate, this method applies the Bonferroni correction. Given that the total number of anomaly regions is 2^n, the p-value is calculated as

$$p_{\mathrm{bonferroni}} = \min(1, 2^n \cdot p_{\mathrm{naive}}).$$

- `permutation`: This method uses a permutation test with the steps outlined below:

- Calculate the observed test statistic z^{obs} by applying the observed image $\boldsymbol{x}$ to the diffusion model.
- For each $i = 1, \ldots, B$, compute the test statistic $z^{(i)}$ by applying the permuted image $\boldsymbol{X}^{(i)}$ to the diffusion model, where B represents the total number of permutations, set to 1,000 in our experiments.

$$p_{\text{permutation}} = \frac{1}{B} \sum_{b \in [B]} \mathbf{1}\{|z^{(b)}| > |z^{\text{obs}}|\},$$

where $\mathbf{1}\{\cdot\}$ denotes the indicator function.

D Architecture of the U-Net

Figure 6 shows the architecture of the U-Net used in our experiments. The U-Net has three skip connections, and the Encoder and Decoder blocks. For image sizes $n \in \{64, 256, 1024, 4096\}$, the corresponding spatial dimensions of images are $(1, d, d)$ where $d \in \{8, 16, 32, 64\}$.

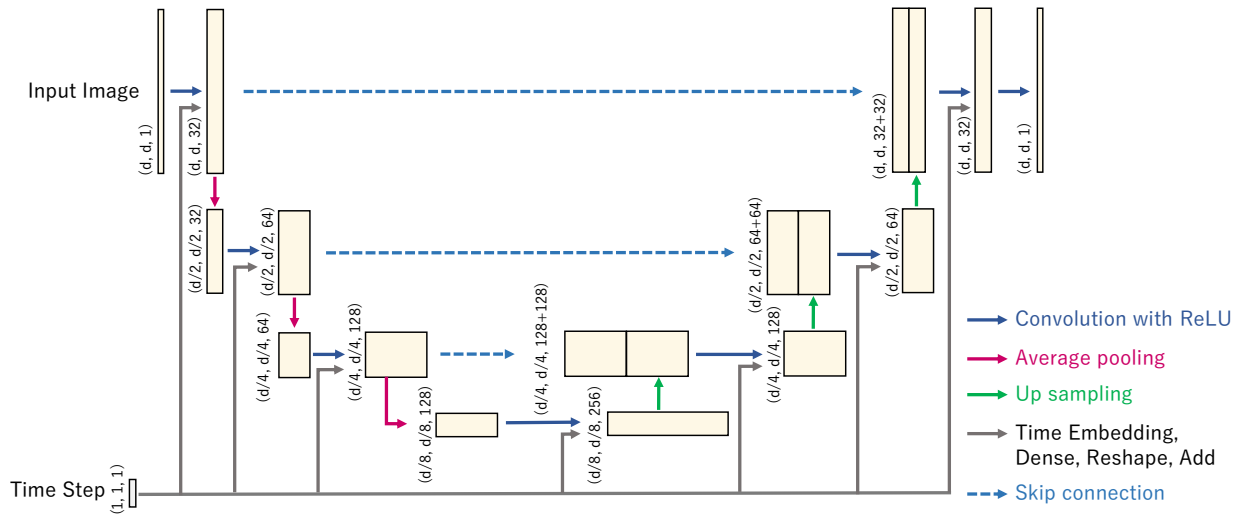

Figure 6: The architecture of the U-Net

E Accelerated reverse processes

Methods for accelerating the reverse process have been proposed in DDPM, DDIM (Song et al., 2022). When taking a strictly increasing subsequence τ from $\{1, \cdots, T\}$, it is possible to skip the sampling trajectory from $\mathbf{x}_{\tau_i}$ to $\mathbf{x}_{\tau_{i-1}}$. In this case, equations (2) and (4) can be rewritten as

$$\mathbf{x}_{\tau_{i-1}} = \sqrt{\alpha_{\tau_{i-1}}} \left(\frac{\mathbf{x}_{\tau_i} - \sqrt{1 - \alpha_{\tau_i}} \cdot \epsilon^{(\tau_i)}(\mathbf{x}_{\tau_i})}{\sqrt{\alpha_{\tau_i}}} \right) + \sqrt{1 - \alpha_{\tau_{i-1}} - \sigma_{\tau_i}^2} \cdot \epsilon_\theta^{(\tau_i)}(\mathbf{x}_{\tau_i}) + \sigma_{\tau_i} \epsilon_{\tau_i},$$

where

$$\sigma_{\tau_i} = \eta \sqrt{(1 - \alpha_{\tau_{i-1}})/(1 - \alpha_{\tau_i})} \sqrt{1 - \alpha_{\tau_i}/\alpha_{\tau_{i-1}}}.$$

Therefore, piecewise-linearity is preserved, making the proposed method DAL-Test applicable.

F Experimental settings for the real-world datasets

F.1 Experimental settings of Brain Tumor Segmentation 2023 dataset

We evaluate our method on T2-FLAIR MRI brain scans from the Brain Tumor Segmentation 2023 dataset (Karargyris et al., 2023; LaBella et al., 2023). T2-FLAIR MRI comprises 934 non-skull-stripped 3D scans with dimensions of $240 \times 240 \times 155$. From these scans, we extracted 2D 240×240 axial slices at axis 95, resized them to 64×64 pixels, and categorized them based on the anomaly annotations into 532 normal images (without tumors) and 402 abnormal images (with tumors). For each scan, we estimated the mean and variance from pixel values excluding both the non-brain regions and tumor regions identified in the ground truth, followed by standardization. We randomly selected 312 normal images for model training. The model was trained with $T = 1000$ and the initial time step of the reverse process was set at $T' = 300$, with reconstruction performed through 5 step samplings. We set the threshold $\lambda = 0.6$ and the kernel size of the averaging filter to 3. Note that, when testing images of the MRI brain scans, the non-brain regions are not treated as anomalous regions $\mathcal{M}_{\boldsymbol{X}}$.

F.2 Experimental settings of MVTec AD dataset

We evaluate our method on the MVTec AD dataset (Bergmann et al., 2019), which consists of 15 object categories. Each category provides a training set of normal images and a test set containing both normal and abnormal images, with image resolutions ranging from 900×900 to 1024×1024 pixels. For our experiments, we select four categories (bottle, cable, grid, transistor) and resize all images to 128×128 pixels. For the type I error rate experiments, we randomly select 50 normal images from each category, and for the power experiments, we select 50 abnormal images per category. The diffusion model is trained on the remaining normal images with $T = 1000$ total diffusion steps, of which the first $T' = 300$ steps are used for reconstruction using 4 sampling steps. We apply an averaging filter with a kernel size of 3. We set the anomaly threshold λ to 1.0 for bottle and to 1.2 for cable and grid. In the power experiments, we compute the intersection between the anomalous region detected by the diffusion model and the anomaly annotation. Since the images in the MVTec AD dataset are RGB, we redefine the image data as $\tilde{\boldsymbol{X}} \in \mathbb{R}^{hw \times 3}$, where h and w denote the image height and width. We then vectorize each image by

$$\boldsymbol{X} = \mathrm{vec}(\tilde{\boldsymbol{X}}) = (X_{1,1}, X_{1,2}, X_{1,3},\ X_{2,1}, X_{2,2}, X_{2,3}, \ldots, X_{hw,1}, X_{hw,2}, X_{hw,3})^\top \in \mathbb{R}^n,$$

Similarly, we define the reference image $\tilde{\boldsymbol{X}}^{\mathrm{ref}} \in \mathbb{R}^{hw \times 3}$ as the average of the training images, and vectorize it in the same way as above.

$$\boldsymbol{X}^{\mathrm{ref}} = \mathrm{vec}(\tilde{\boldsymbol{X}}^{\mathrm{ref}}) = (\tilde{X}_{1,1}, \tilde{X}_{1,2}, \tilde{X}_{1,3},\ \tilde{X}_{2,1}, \tilde{X}_{2,2}, \tilde{X}_{2,3}, \ldots, \tilde{X}^{\mathrm{ref}}_{hw,1}, \tilde{X}^{\mathrm{ref}}_{hw,2}, \tilde{X}^{\mathrm{ref}}_{hw,3})^\top \in \mathbb{R}^n$$

where $n = 3hw$, and accordingly redefine the test statistic in (7) as

$$T(\boldsymbol{X}, \boldsymbol{X}^{\mathrm{ref}}) = \frac{1}{|\mathcal{M}_{\boldsymbol{X}}|} \sum_{i \in \mathcal{M}_{\boldsymbol{X}}} \sum_{j \in [3]} \tilde{X}_{i,j} - \frac{1}{|\mathcal{M}_{\boldsymbol{X}}|} \sum_{i \in \mathcal{M}_{\boldsymbol{X}}} \sum_{j \in [3]} \tilde{X}^{\mathrm{ref}}_{i,j}$$

With this setup, our method can be applied in the same way as in §3.